International Journal of Fatigue 119 (2019) 160–172

Contents lists available at ScienceDirect

International Journal of Fatigue

journal homepage: www.elsevier.com/locate/ijfatigue

Fatigue properties of AlSi10Mg produced by Additive Layer Manufacturing

Julius N. Domfang Ngnekou[a,b], Yves Nadot[a], Gilbert Henaff[a], Julien Nicolai[a], Wen Hao Kan[c], Julie M. Cairney[c], Lionel Ridosz[b]

[a] *Institut Pprime, Département de Physique et de Mécanique des Matériaux, ENSMA-CNRS-Université de Poitiers, 1 avenue Clément Ader, Téléport 2, 86960 Chasseneuil-Futuroscope, France*
[b] *Zodiac Aerospace, 61 rue Pierre Curie, 78370 Plaisir, France*
[c] *Aerospace, Mechanical and Mechatronic Engineering, The University of Sydney, Australia*

ARTICLE INFO

Keywords:
ALM
AlSi10Mg
Fatigue
Kitagawa
T6

ABSTRACT

This work shows the impact of microstructure and defect on the fatigue life of an AlSi10Mg manufactured by Additive Layer Manufacturing (ALM). Samples were manufactured via a laser powder-bed process: two configurations (0° and 90°) are considered in order to evaluate the impact of the building direction on fatigue properties. 3D X-Ray tomography was used to characterize the defect population. The microstructure was characterized by considering four parameters: melt-pools, crystallographic grains, dendritic structure and precipitates. The fatigue properties were determined by establishing S-N curves for machined samples, with and without T6 heat-treatment, at $R = -1$ under tensile loading. The size of the defect responsible for the fatigue failure was determined in each sample so as to establish a relationship between the fatigue limit and the defect size using Kitagawa-type diagrams. In order to study a broader range of defect size, artificial defects were introduced using electro-discharge machining. The following observations are made: (i) after heat-treatment, the boundaries of melt-pools and the dendritic structure are not visible. Si is organized into pure precipitates homogeneously distributed over space and intermetallic Fe based compounds are observed in the form of needles; (ii) The impact of building direction on fatigue life is seen only after T6 heat treatment; (iii) An improvement of the fatigue resistance is observed after T6, in spite of the presence of intermetallic needles; (iv) The fatigue limit is controlled by the defect size both before and after T6 heat treatment, and it seems that the influence of T6 decreases as the defect size increases.

1. Introduction

Additive manufacturing is considered to be a disruptive technology, offering the possibility of producing topographically optimized parts with a complex shape [1–6]. It is changing the nature of manufacturing in fields such as biomaterial, automotive and aeronautical engineering. In the aeronautical context, the introduction of such an innovative process would require material qualification in which the control of the fatigue resistance is crucial [7–9]. It is, therefore necessary to understand the relationship between the microstructure inherited from the manufacturing process and the fatigue behavior. The impact of the heat treatment is also important. This information will enable the building strategy to be optimized to maximize the local fatigue resistance. In this work, the relationship between microstructure, the defect and the fatigue behavior is addressed for the case of an AlSi10Mg alloy produced by the Additive Layer Manufacturing (ALM) process.

Many studies on AlSi10Mg alloy have focused on the characterization of specimens machined from built parts [10–14], and this has led to a quantitative description of the microstructure along five characteristic parameters: (i) the melt-pools, (ii) the dendritic structure, (iii) the grains, (iv) the precipitation structure and (v) the defect population. It has been observed that melt-pools, dendritic structure and grains are strongly anisotropic depending on the building direction [14].

According to Domfang et al. [13], after a T6 heat treatment, the melt-pool boundaries are no longer visible via optical microscopy (without etching) due to the reorganization of the Si phase which provides the surface contrast. Takata et al. [14] observed no influence of T6 heat treatment on the crystallographic anisotropy. Brandl et al. [15] demonstrated the impact of microstructure anisotropy, T6 and platform temperature on fatigue behavior. According to these authors, the impact of the anisotropy from the sample build orientation on the fatigue strength is observed when the building platform is maintained at 30 °C. By coupling a platform temperature of 300 °C and a post-fabrication T6 heat treatment, they found no difference between different growth directions. Maskery et al. [16] evaluated the impact of a T6 heat-treatment on the fatigue performance of samples with an as-built

---

E-mail address: julius.domfang@ensma.fr (W.H. Kan).

https://doi.org/10.1016/j.ijfatigue.2018.09.029
Received 6 July 2018; Received in revised form 26 September 2018; Accepted 30 September 2018

Nomenclature

UTS	ultimate tensile stress (MPa)
YS	yield stress (MPa)
A%	elongation to failure (%)
Ra	arithmetic roughness (µm)
W	mass composition (%)
DAS	Dendritic Arm Spacing (µm)
SDAS	Secondary Dendritic Arm Spacing (µm)
A	Basquin coefficient
R	load ratio
σ_{D-1}^{ten}	fatigue limit for alternating tension at R = −1 (MPa)
N_f	number of cycle at failure
α	Basquin slope
σ_n	stress amplitude at step n (MPa)
σ_{n-1}	the stress amplitude at step n − 1 (MPa)
σ_{max}	maximum stress in load direction (MPa)
s	sphericity factor (between 0 and 1)
A_{3D}	area of the envelope of the defect on the fracture surface (µm^2)
V_{3D}	volume of the defect (µm^3)
$\sqrt{area}$	defect size defined by Murakami, measured on the fracture surface (µm)

manufactured surface and showed that the T6 treatment improved the fatigue limit. Aboulkhair et al. [17] also showed that the T6 heat treatment improves the fatigue resistance but only to a small degree. As the additive manufacturing process involves numerous parameters that potentially affect the microstructure and the residual stresses, it is important to bring up the material to a standardized microstructure so that one material can be compared to another. In that purpose, for aluminum alloys, the microstructure following a T6 heat treatment can be considered as a reference for this type of process.

However, only a few studies so far have quantified the specific impact of defect size on the fatigue limit. Beretta and Romano [18] recently published a literature survey on this topic, analyzing the impact of defect size on fatigue limit by means of Kitagawa-type diagrams. The fatigue limit obtained on machined samples fatigued at R = −1 was compared to the one determined for a cast Al-Si alloy with different Secondary Distance Arms Spacing values (SDAS). It appears that the ALM material is a little more tolerant to defects than the cast alloy. At R = 0.1, according to Romano et al. [19], and based on results on machined surfaces [20,21], the selectively melted AlSi10Mg is as defect-tolerant as the equivalent cast heat-treated alloy. According to Maskery et al. [16], when ALM samples are tested with an as-built surface, the relative drop in fatigue resistance could reach 40%.

In this work, the impact of defect size on the fatigue limit is studied for as-machined samples with and without T6 heat treatment, by decoupling the effect of the microstructure anisotropy. The approach consists of the evaluation of the fatigue resistance of XY and Z machined samples with or without T6. Firstly, the S-N curves at R = −1 are established, and thereafter the fatigue limit is quantified by a step-by-step method as a function of defect size. After the identification and characterization of the critical defect on the fracture surface, the Kitagawa diagram is plotted and discussed for the materials being studied.

2. Experimental details

2.1. Material and samples

Specimens were fabricated by the ALM method using a pre-alloyed powder with an average particle size of 30 µm. Two distinct productions from two different machines, labeled P1 and P2, are considered in the present study. The chemical competition used in both P1 and P2 powder are in accordance with the DIN EN 1706:2010 standard.

For the P1 production, the fabrication was operated under deliberately sub-optimal parameters. The layering in such a case is performed by means of a scraper. All P1 specimens have been machined from XY bars built on an aluminum platform maintained at 150 °C. In order to release the stresses induced by the process, one hour post-processing heat treatment was performed at 210 °C.

For P2 production, the bars were fabricated by operating the machine under standard optimized parameters. The layering stage of the

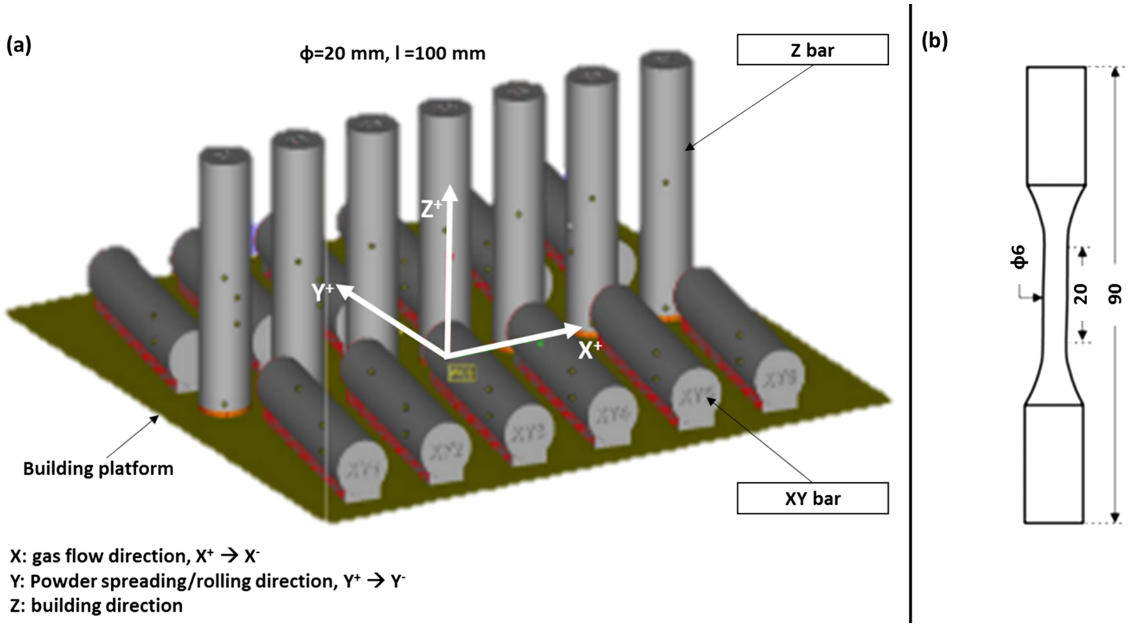

Fig. 1. (a) Position and orientation on the building platform of bars from which fatigue specimens are machined, (b) Fatigue test specimen geometry, one bar corresponds to one specimen.

Table 1
A comparison of the DIN EN specifications of AlSi10Mg and the composition of the studied alloy measured by EDS.

	Al	Si	Fe	Mg	Mn	Zn	T
DIN EN 1706:2010	Bal	9–11	< 0.55	0.2–0.45	< 0.45	< 0.1	< 0.15
W% EDS measure	Bal	9.55		0.4			

Table 2
T6 conditions.

Steps	Temperature (°C)	Duration (h)	Environment
Solid solutioning	540	8	Air
Quenching	20		Water
Tempering 1	20	24	Air
Artificial ageing	160	10	Air

Table 3
Designation of each individual fatigue specimen is used in this paper, depending on the production number, the orientation and whether or not a T6 treatment was applied.

Production	Platform temperature (°C)	Post process heating (°C)	Orientation	T6	Designation	Ra
P1	150	210	XY	No	P1-XY-MA	/
P2	200	300	XY	No	P2-XY-MA	0.7
				Yes	P2-XY-MA-T6	1.2
			Z	No	P1-Z-MA	1.0
				Yes	P2-Z-MA-T6	1.0

process is also performed by means of a scraper. P2 bars were built in two directions, namely XY and Z as defined in Fig. 1a. The platform was maintained at 200 °C and the recommended two hours stress relaxation treatment was performed at 300 °C.

The bars built in both P1 and P2 productions suffer from surface integrity effects such as the roughness and an expected population of under-layer defects due to edge lasing [22,23]. Thus, for both P1 and P2 productions, the fatigue test specimens were machined (MA) from these bars in order to avoid the aforementioned process-induced surface effects. The fatigue test specimen geometry is shown in Fig. 1b. The samples were tested in the as-machined condition, with no surface polishing. After machining, some specimens were subjected to a T6 heat treatment under the conditions listed in Table 2. Table 3 indicates the different conditions in which the samples where produced and heat-treated.

In order to characterize the material, cubic samples were removed from the bars using electric discharge machining (EDM) and polished along three orthogonal directions using SiC paper (1000, 2000, and 4000 grades) and then with diamond suspensions (3 µm and 1 µm size). Microstructural characterization of these cubic samples was carried before and after heat treatment (HT). The surfaces were then observed using an optical microscope without etching. The chemical composition and the microstructure of the samples were studied using a JEOL-7001F-TTLS (with operating voltage of 5–30 kV) high resolution scanning electron microscope (SEM), equipped with secondary and back-scattered electron detectors and energy dispersive X-ray spectrometer (EDS). So, the composition of the specimen at the surface was quantified using EDS. As reported in Table 1, the composition determined is in accordance with the DIN EN 1706:2010 standard. Using EDS technique, the non-detection of some elements, especially that of Fe and Mn, confirms that the materials are within the recommended specifications as they would have been detected if they were in amounts exceeding their allowable limits. The local structure of the material was studied by transmission electron microscopy (TEM) using a JEOL 2200FS equipped with an omega filter. TEM samples were prepared using focused ion beam (HELIOS-Dual Beam) equipped with an electron backscatter diffraction (EBSD) detector.

In order to characterize the crystallographic orientation of grains, each sample was first cold-mounted in epoxy resin and ground by using SiC abrasive papers. Those samples was then fine polished using 3 µm and 1 µm diamond suspensions followed by OP-S colloidal silica suspension. The morphology and orientation of Al grains were characterized by EBSD technique. Each EBSD scan was conducted on a Zeiss Ultra field emission gun scanning electron microscope equipped with an EBSD detector was used for the EBSD scans using the following condition: an accelerating voltage of 20 kV, a step-size of 0.8 µm, an aperture of 120 µm, and a scan area of 600 µm × 600 µm. The indexing rates for all scans were above 90%. The data analysis was carried out using Oxford Instruments HKL Tango and Mambo software. Each dataset was cleaned by applying wild spikes and 3-nearest neighbours once. A 10° misorientation angle and a grain boundary completion angle down to 0° were both used to define grain boundaries. If a section (s) of a grain was found to lie outside the borders of the

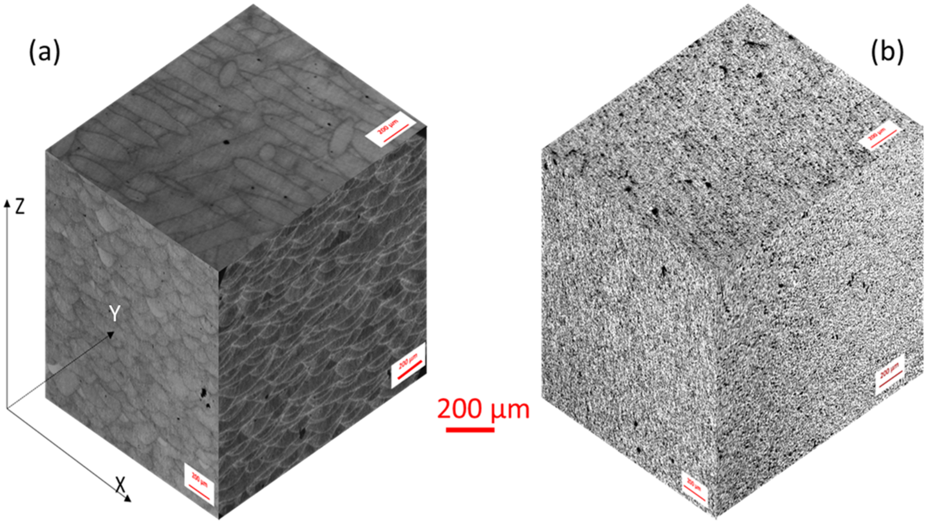

Fig. 2. Optical dark field microscopy 3D reconstructions of the microstructure after surface polishing, without etching, (a) without heat treatment (b) after T6.

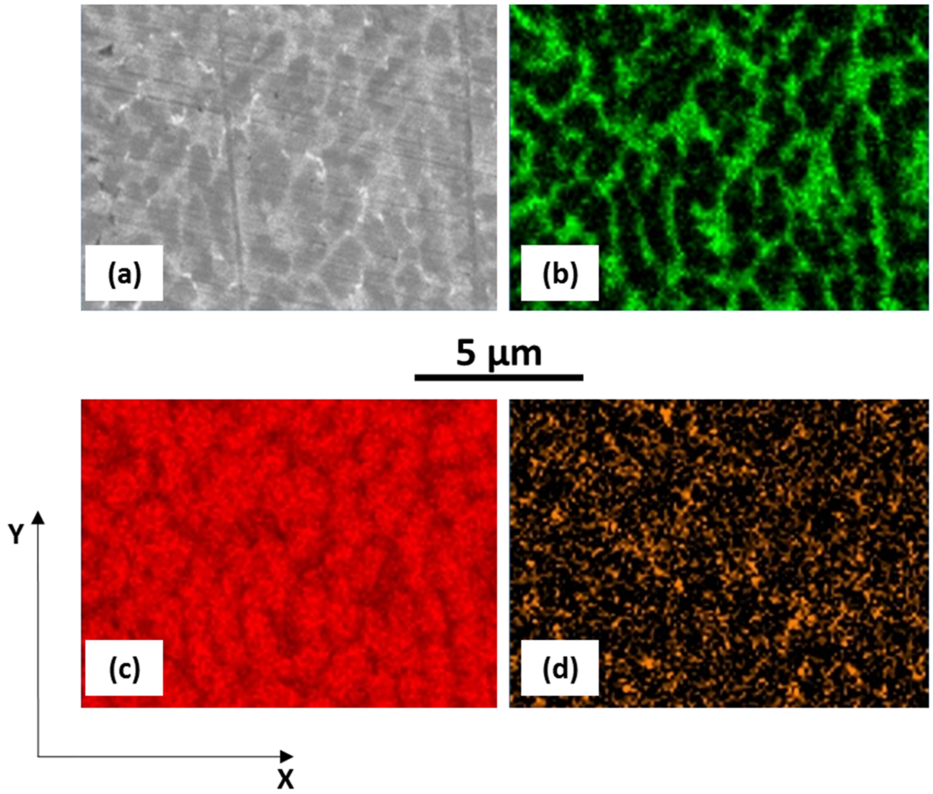

Fig. 3. (a) SEI image without mapping. EDS chemical maps of elements present in the alloy without T6. Distribution of (b) silicon (green), (c) aluminium (red), (d) Magnesium (orange). (For interpretation of the references to colour in this figure legend, the reader is referred to the web version of this article.)

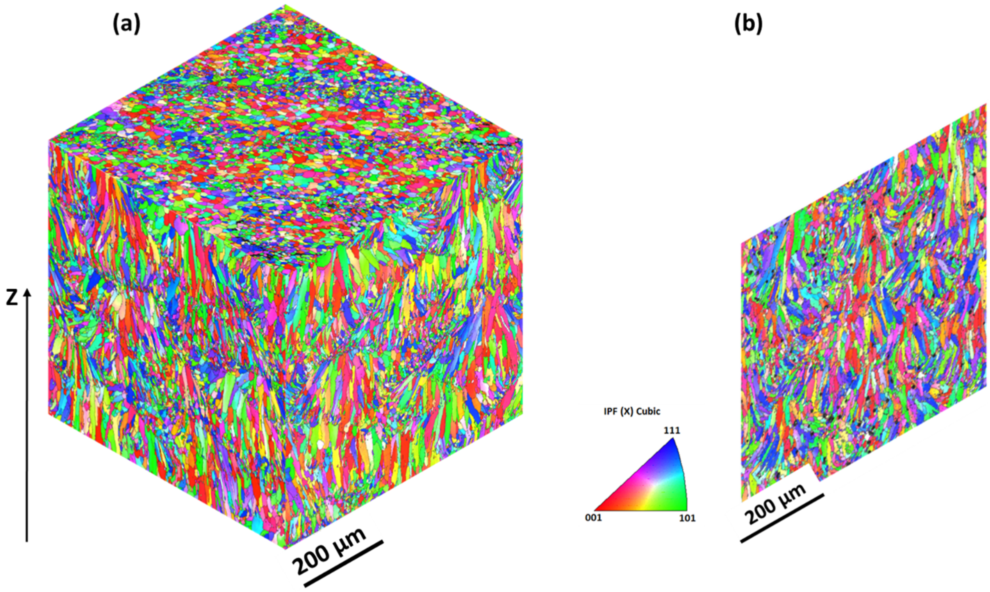

Fig. 4. EBSD observations of the grain orientation, (a) 3D observation before T6 heat treatment, (b) XZ image after T6 heat treatment.

600 µm × 600 µm EBSD scan area (i.e. the grain is incomplete), its grain size was then approximated by multiplying the calculated grain size by a factor of 2 (if it intersects one border), or a factor of 4 (if it intersects two borders).

Finally, in order to characterize the defect population, two cylindrical specimens of 3 mm diameter and 10 mm length were machined from the gauge section of the fatigue test samples. These samples were analyzed by X-ray UltraTom® tomography with the following configuration: a 150 kV source with a resolution of 5 µm per voxel. The analysis of the defect distribution in the bulk of the samples was carried out with the commercial software Avizo®.

2.2. Mechanical testing

Tensile tests were carried out in accordance with the standard NF EN 10002-1, using an Instron 4505 load-frame with a displacement rate of 0.22 mm/min at room temperature. The elongation was measured by an extensometer, with a gauge length of 12.5 mm. Two samples were tested for each condition. Vickers micro hardness was also measured in the core of each P2 samples as an average of 16 indentations under a

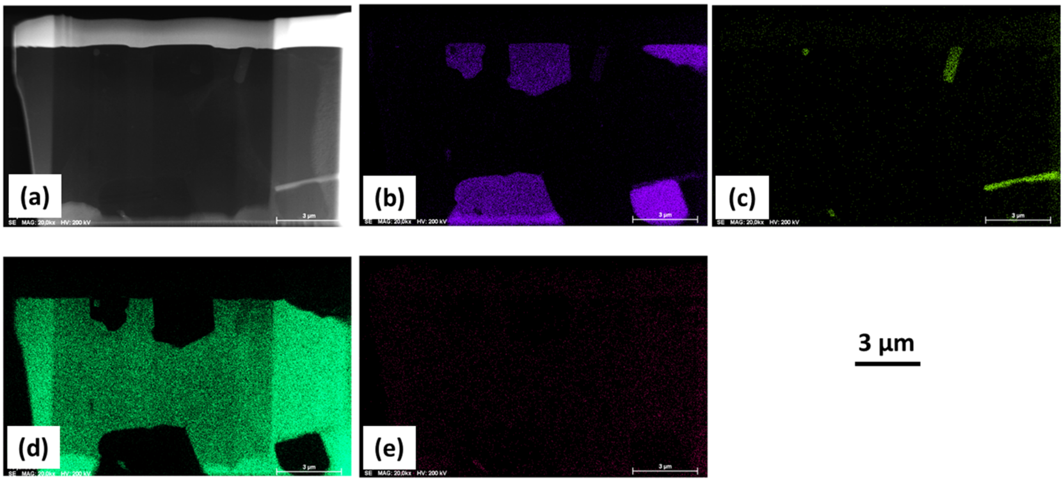

Fig. 5. (a) TEM micrograph on T6 sample and EDS mapping of chemical elements. Distribution of (b) silicon (purple), (c) Iron (yellow), (d) aluminium (green), (e) Magnesium (orange). (For interpretation of the references to colour in this figure legend, the reader is referred to the web version of this article.)

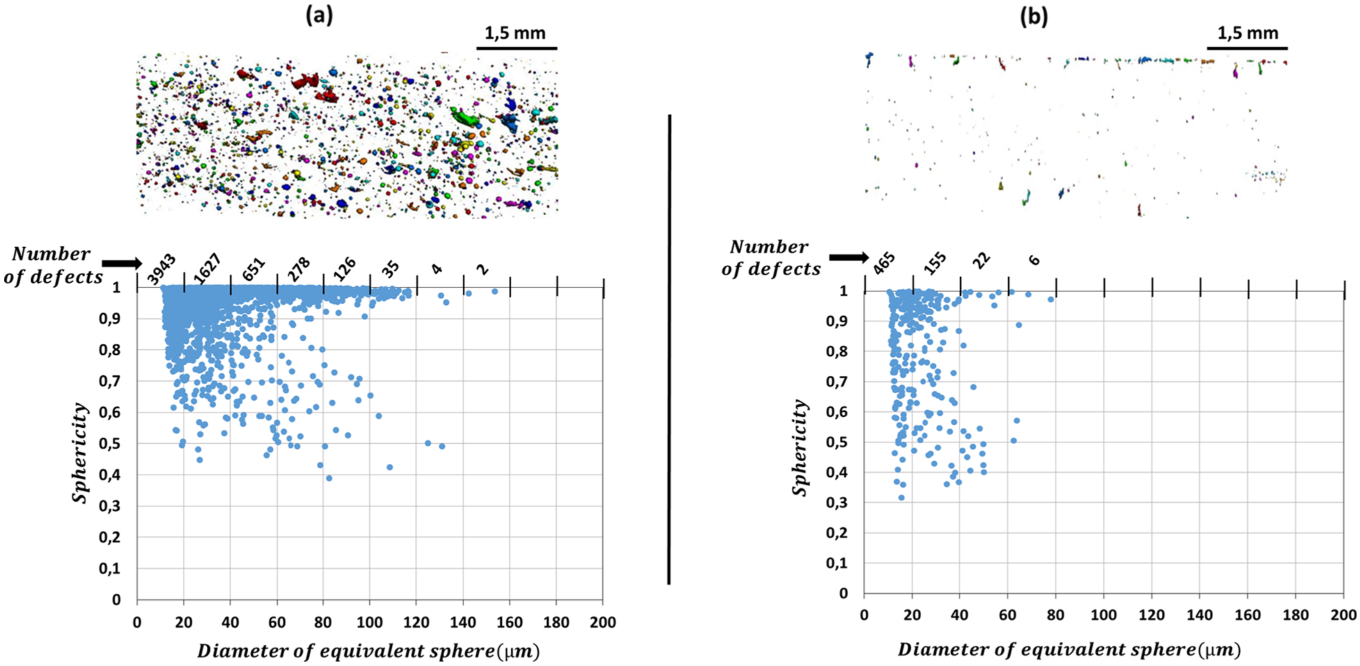

Fig. 6. Defect characterization of P1 and P2 production. The top images give the special repartition of defects in observed zone while bottom show the number of defect and sphericity distribution related to the equivalent diameter (a) P1 production, (b) P2 production.

50 mN load.

Fatigue tests were conducted at room temperature on a resonance machine at a frequency of 80 Hz and a load ratio of R = −1. A 5 Hz drop in frequency was considered as a criterion for failure detection. This drop corresponds to a crack depth of half the diameter of the specimen. The fatigue limit is defined as the amplitude of load, that is to say, the maximum load minus the average load. In this study, a step-by-step method described by Iben Houria et al. [24] was used to determine the fatigue limit at 10^6 cycles. This is the only way to evaluate the fatigue limit in presence of a natural defects. It is assumed that no significant loading history effect is introduced by the loading steps applied prior to the step leading to failure, as shown by Roy et al. [25] for the case of a A356 cast Al-alloy. In order to plot a Kitagawa-type diagram, the fatigue limit is determined for each specimen using the following rules:

- when the specimen fails during the first step, a Basquin equation is used to evaluate the fatigue limit. The parameters of Basquin equation are determined via experimental points on the S-N curves averaged by the least-squares method.

$$\sigma_{D-1}^{ten} = A\cdot N_f^{\alpha} \tag{1}$$

- when the specimen fails after one or several loading steps, the fatigue limit is determined by a linear interpolation according to the following equation:

$$\sigma_{D-1}^{ten} = \frac{N_f}{10^6}\cdot(\sigma_n - \sigma_{n-1}) + \sigma_{n-1} \tag{2}$$

Residual stresses were quantified using the X-ray diffraction according to the AFNOR NF EN 15305 standard. The measurement of residual stresses were performed at the surface of samples after fatigue loading. These measurement were carried out at the surface, in the axial and circumferential direction. The point of analysis is furthermore placed as far as possible from the fracture surface of the specimen. Four

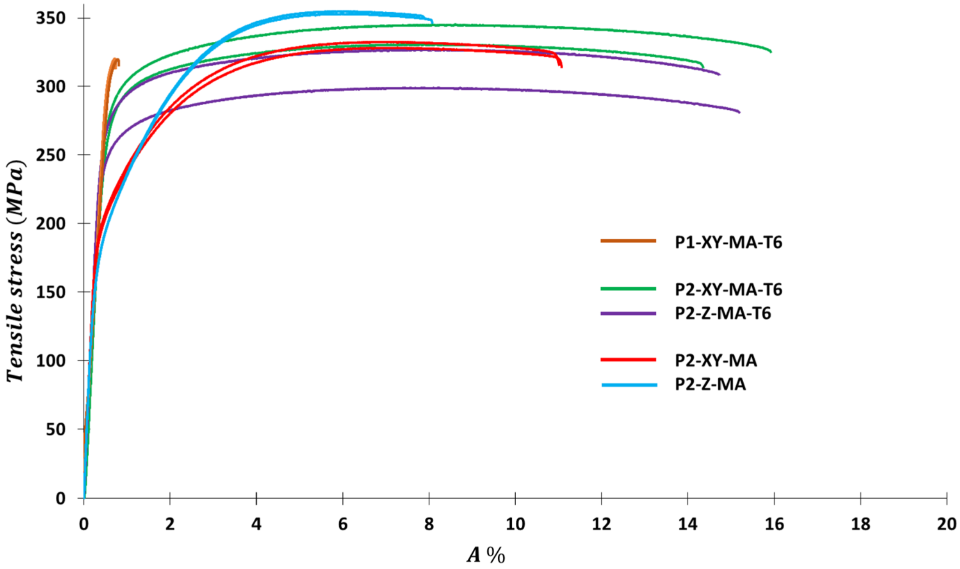

Fig. 7. Influence of the building direction and T6 heat treatment on the tensile properties of ALM AlSi10Mg alloy.

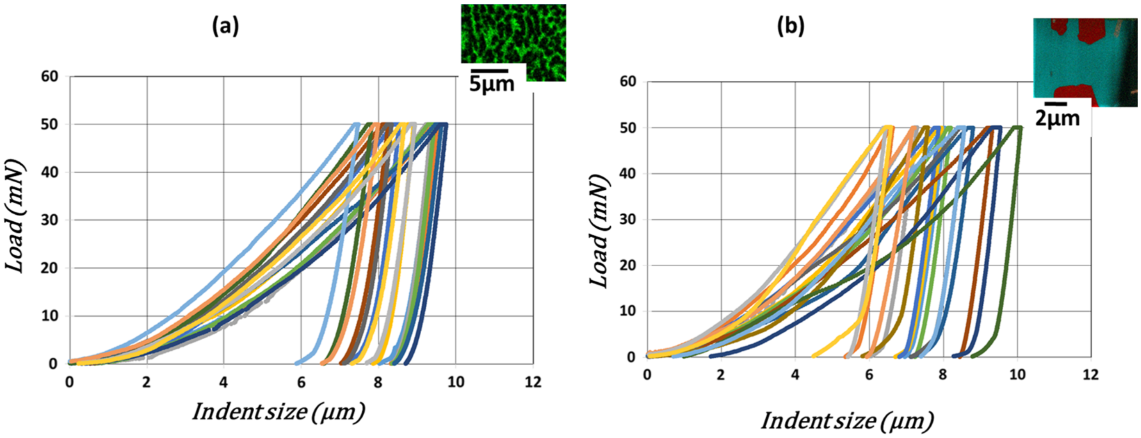

Fig. 8. Micro hardness characterization of P2 material. Load and discharge curves. (a) no T6, (b) after T6.

specimens were considered: two in the XY direction, and two in the Z direction. For both pairs of samples, one was not subjected to a T6 heat treatment.

3. Results

3.1. Microstructure

The microstructure of the P2 material was characterized along the four main characteristic features, namely: *the melt-pools* (1), *dendritic structure* (2), *crystallographic grain* (3), and *silicon precipitates and intermetallic needles* (4).

(1) The *melt-pools*, which can be geometrically described by their length, width and height. These melt-pools reflect the imprint generated by the laser beam during the melting of the deposited powder. As shown in Fig. 2a, these melt-pools are strongly anisotropic in shape. The mean dimensions of the melt-pool are (length: 600 µm, width: 150 µm and height in the Z direction: 80 µm). A previous study of the melt-pool boundaries by Thijs et al. [10] reported that the melt-pools consist of an heterogeneous distribution of eutectic silicon in the alpha-phase of aluminum. In Fig. 2b it can be seen that, after T6 heat treatment, the melt-pool boundaries are no longer visible, presumably due to the demixing and coalescence of silicon in the aluminum matrix at sub-eutectic temperatures. According to Li et al. [26], a high solution-annealing temperature in the range of 450–550 °C leads to coarse distribution of silicon particles, typically around 2–4 µm. Additional growth of these particles was seen during artificial aging.

(2) The *dendritic structure*, shown in Fig. 3 (taken along the scanning plane), is characterized by the size of the α-Al matrix surrounded by eutectic silicon. The rapid solidification involved in the ALM process does not allow the formation of a dendritic structure with secondary arms, contrary to cast aluminum alloys. In this study, a Dendritic Arm Spacing (DAS) was observed to be between 0.5 and 2 µm, which is significantly smaller than the characteristic SDAS parameter in cast Al-Si alloys (30–100 µm depending on the cooling rate). Previous studies have shown that this parameter has a large influence on the fatigue behavior [25,27–31]. According to Wang et al. [31], in the absence of defects a refined SDAS leads to the high fatigue life.

(3) Fig. 4 shows that the morphology of the *crystallographic grains* is

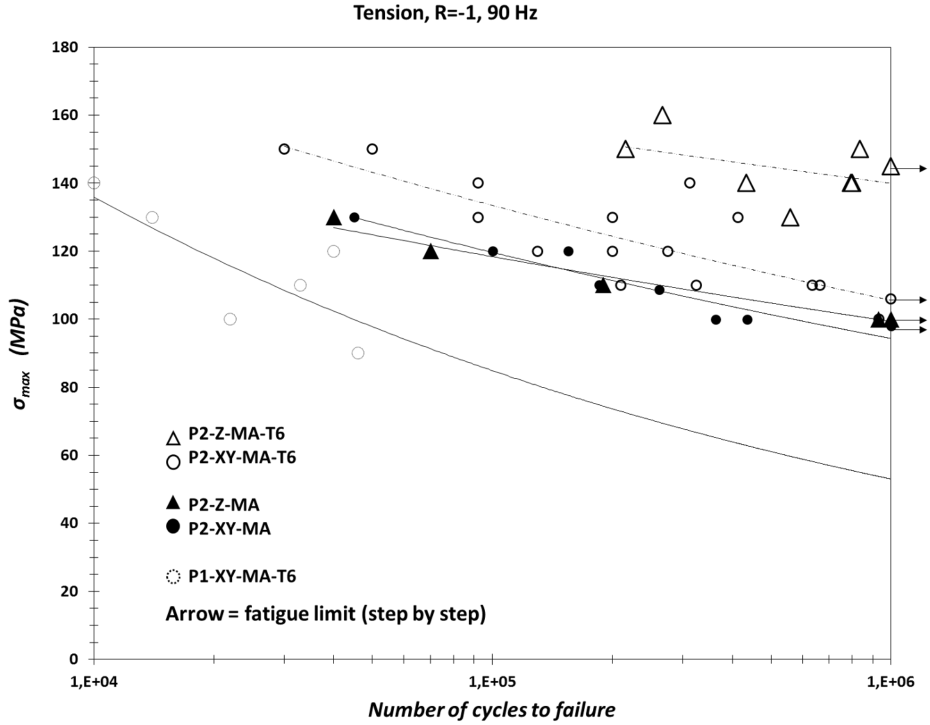

Fig. 9. Influence of the building direction, process parameters and T6 heat-treatment on the fatigue properties.

Table 4
Residual stresses measurement.

	Axial stress (MPa)	Circumferential stress (MPa)
P2-XY-MA	4	8
P2-Z-MA	−13	−11
P2-XY-MA-T6	−39	−55
P2-Z-MA-T6	−17	−26

strongly anisotropic, and those grains were seem to grow epitaxially towards the centers of the melt-pools, as previously observed by Thijs et al. [10]. The grain growth was observed to encompass one to three melt pools. In Fig. 4, the impact of T6 heat treatment can be observed. The T6 heat treatment does not strongly affect the grain structure; this observation is in agreement with the previous observations made by Takata et al. for AlSi10MgSi alloy prepared by ALM [14] and by Wang et al. for cast A356 [31].

(4) *Silicon precipitates and iron-rich needles* are observed in the structure after T6 heat treatment as seen in Fig. 5b and c. In fact, during the heat treatment, the diffusion and segregation of Si and Fe atoms occurs, leading to the formation of Fe-rich precipitates and Si crystals randomly distributed in the Al-matrix. A thin foil was analyzed using EDS technique, revealing that particles such as the one exhibited in Fig. 5b contain 98% silicon (Si) and only 2% of aluminum (Al). The same EDS technique reveals that needled-shaped component on Fig. 5c contains on average 10% iron (Fe), 41% aluminum (Al) and 49% silicon (Si).

3.2. *Defect population*

The defect population was characterized using the computed X-ray tomography. The sources images was segmented by gray level. The defects was then extracted and analyzed. The top images in Fig. 7 show that both P1 and P2 production leads to numerous and randomly distributed defects. P1 production contains 6666 defects while P2 contents 648 for the same volume sampled. It also suggested in Fig. 7 that the defect shape can be different, so that for each defect, the shape was quantified using a sphericity index defined as follows:

$$s = \frac{\pi^{\frac{1}{3}}\cdot(6V_{3D})^{\frac{2}{3}}}{A_{3D}} \tag{3}$$

A sphericity index of 1 represents the case of a pure spherical defect [23]. The defect size is given by the diameter of the equivalent sphere. Thereby, sphericity index was plotted as a function of the defect size for P1 and P2 productions as shown in Fig. 6. The P1 production leads to defects two times larger than the P2 production. Fig. 6 further indicates that the process parameters used for processing both P1 and P2 samples leads to the formation of mostly spherical defects, except for some large defects where the shape is not represented by a sphere.

3.3. *Tensile properties and hardness*

Fig. 7 presents engineering stress-strain curves for the P1 and P2 productions. From these curves, the mechanical properties such as UTS, A% and YS were derived and are reported in Table 5**.** For the non-heat-treated materials, it is observed that the UTS value is higher for Z samples compared to XY. After T6 heat treatment, the UTS shows a scatter in the range of 300–345 MPa, and, a strong reduction of the ductility of P1 production is noticed. For non-heat treated samples**,** the building direction strongly impacts the tensile elongation A% whereas the yield stress (YS) is not strongly affected. For P2 production, after the T6 heat treatment, there is no major difference in the ductility (A%) for both XY and Z samples. In addition, an increase in hardness of the material followed by an increase in yield stress is observed. This increase of micro-hardness after the T6 heat treatment, diminishes the work hardening capability of the material for P2 production, regardless

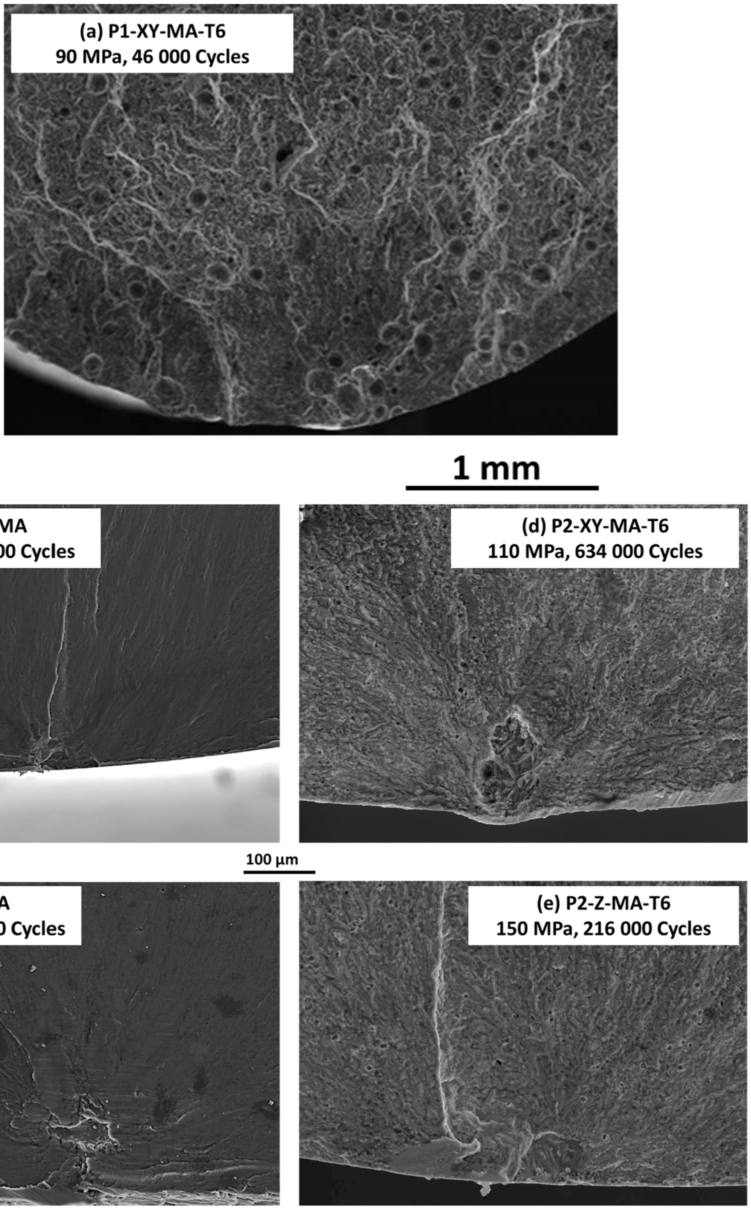

Fig. 10. SEI images of fracture surfaces and initiation sites. (a) P1-XY-MA-T6, (b) P2-XY-MA, (c) P2-Z-MA, (d) P2-XY-MA-T6 and (e) P2-Z-MA-T6.

of the building direction. Likewise, the T6 heat treatment leads to a large scatter in hardening. Fig. 8 shows that the indent size varies between 7 and 10 µm without heat treatment and is reduced to 5 µm after heat treatment.

3.4. S-N curves

Fig. 9 presents the S-N curves for P1 production with only XY samples that was subjected to the T6 heat treatment, and P2 production with XY and Z samples, with and without T6. Symbols with arrows indicates the fatigue limit determined at one million cycles by the step-by-step method while each other symbols correspond to sample failure. There is no significant difference on the fatigue resistance between the P2-XY-MA and P2-Z-MA samples. A 20% increase in the fatigue limit is observed for P2-XY-MA in comparison to P2-XY-MA-T6, while more than 45% is observed for P2-Z-MA-T6 in comparison to P2-Z-MA. Compared to P1-XY-MA, the fatigue limit of the P2-XY-MA samples is improved by about 40%. Examination of the fracture surfaces, as shown in Fig. 9, suggests that the significant increase in fatigue limit between P1 and P2 is due to a reduction in the critical defect size. An increase in the fatigue resistance is observed after T6 despite the presence of iron needles, which is known to degrade the fatigue properties in cast Al-Si alloys [38]. As P2 specimens contain the same type of critical defects and negligible residual stresses (see Table 4), this improvement in fatigue strength after heat treatment can be attributed to the strengthening of the matrix via the applied T6 treatment. However, it is also observed that such a peak hardening treatment leads to a highly pronounced difference in fatigue strength between XY and Z orientations.

3.5. Influence of defect size on the fatigue limit

The examination of the fracture surfaces as shown in Fig. 10, indicates that the fatigue cracks always initiate from a defect. In order to plot the corresponding Kitagawa-type diagram, the defect size was

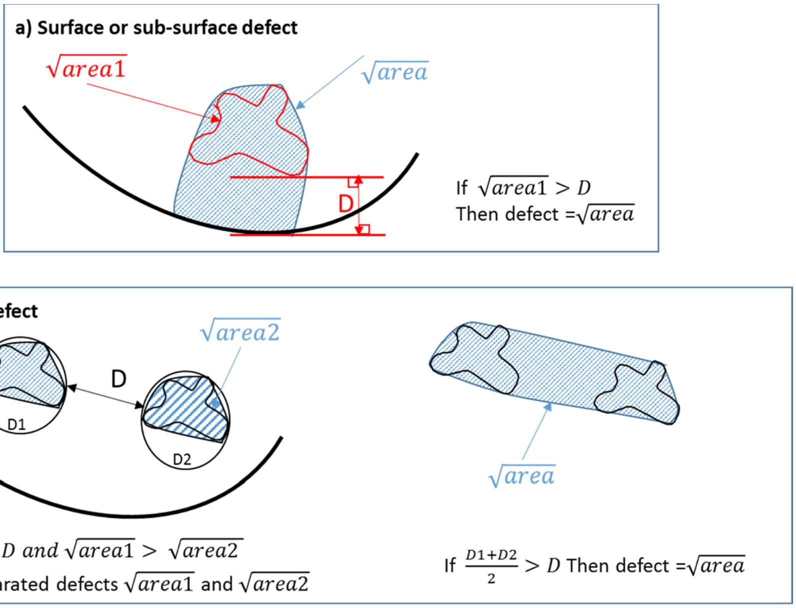

Fig. 11. Definition of the defect size depending on its location relative to the free surface, D1 and D2 are the diameters of a circles that encapsulates the corresponding defect.

assessed using Murakami's parameter($\sqrt{area}$) [39]. Based on Iben Houria works [24], Fig. 11 explains in detail the criteria used to estimate the defect size as a function of its location with respect to the free surface and/or the presence of other defects in the vicinity of the considered defect. Based on this approach, examination of the fracture surfaces indicates that the P2 production introduces pore-type defects ranging from 40 µm to 100 µm. These defects are all located at the specimen surface or in sub-surface. The critical defect size measures by the Murakami parameter is higher than the maximum defect size provided by the tomography analysis. This could be partially explained by the fact that the criterion involve to quantify defect size on the fracture surfaces includes the contribution of the ligaments especially in the case of sub-surface defect.

In Fig. 12, the fatigue limit is plotted as a function of the critical defect size derived from the observation on fracture surfaces. In order to enlarge the scope of this study, artificial spherical defects were introduced by EDM in specimens. For both non-treated and T6 treated materials, this Kitagawa-type diagram confirms that the fatigue limit is mainly sensitive to defect size. These data also confirm the contribution of the anisotropy effect noticed on S-N curves in Fig. 9. The impact of the T6 heat treatment is however less pronounced for larger defects. The Fig. 12 also shows that for a given size of a natural or an artificial defect, there is no influence of defect type on the fatigue limit, so that the results obtained for artificial defects can be extrapolated to natural.

4. Discussion

In this work, the AlSi10Mg alloy elaborated by additive manufacturing were described using five characteristic parameters as presented in the Sections 3.1 and 3.2. This paper exhibits the impact of the T6 heat treatment on the microstructure and it influence on the mechanical properties such as tension, hardness and fatigue.

Concerning the microstructure, it is observed a disappearance of the melt-pools boundaries and the appearance of pure silicon precipitates and iron contained intermetallic. In fact, these are the consequences of the diffusion and coalescence of particles during the heating at high temperature (540 °C) followed by a rapid quenching.

Looking to the tensile properties, as the value of A% is higher for P2 than P1, it is suggested that the loss in the elongation is due to the fact that the P1 production contains much more number of defects than the P2 production. This analysis is consistent with the findings of Kempen et al. [40] who established that the ductility is related to the numbers of defects determined from the analysis of fracture surfaces. Furthermore, according to the theoretical models such as the one proposed by Rice and Tracey [41], the higher the number of defects leads to the higher probability of coalescence of these defect i.e. in A% values. As it is well known that the T6 heat treatment impacts the mechanical properties of aluminum [42], this papers brings the fore the fact that after T6 heat treatment, there is a global increase of A% and all the results of P2 production are equivalent regardless the building direction. This last might be due to the microstructural homogenization due to the T6 heat treatment, as it can be seen in Fig. 2. This explanation suggests that that the obtained microstructure annihilates the potential crystallographic grain impact, as the Fig. 4 shows a strong anisotropy of the grains.

Concerning the micro hardness, a significant increase is noticed on average, which is due to the structural hardening cause by the T6. Table 5 shows that the data present a large scatter after T6 heat treatment. Fig. 5 shows coarse Si particles surrounded by Al. As the silicon is harder than aluminum [43], the presence of those silicon particles surrounded by aluminum explains the fact that the value of micro-hardness differs in the material. The resulting scatter is more important for T6 material than non T6 one, because for T6 material, Si particles are coarser and also the surrounded Al, which would increase the probability to indent in pure Al or in Si.

In terms of fatigue, it was observed that the T6 heat treatment leads to an increase in the fatigue resistance, which is a function of the building directions. According to Brandl et al. [15], the fatigue improvement due to T6 HT is the consequence of the spheroidization of eutectic silicon particles that would limit crack initiation and propagation. However, according to Aboulkhair et al. [17], the T6 HT would reduce the hardness, which would in turn account for the improvement in ductility and fatigue behavior. However, in the present study, it was observed that a T6 HT leads to a 20% increase in hardness for P2-XY samples, which can be correlated to a 20% increase in the fatigue limit.

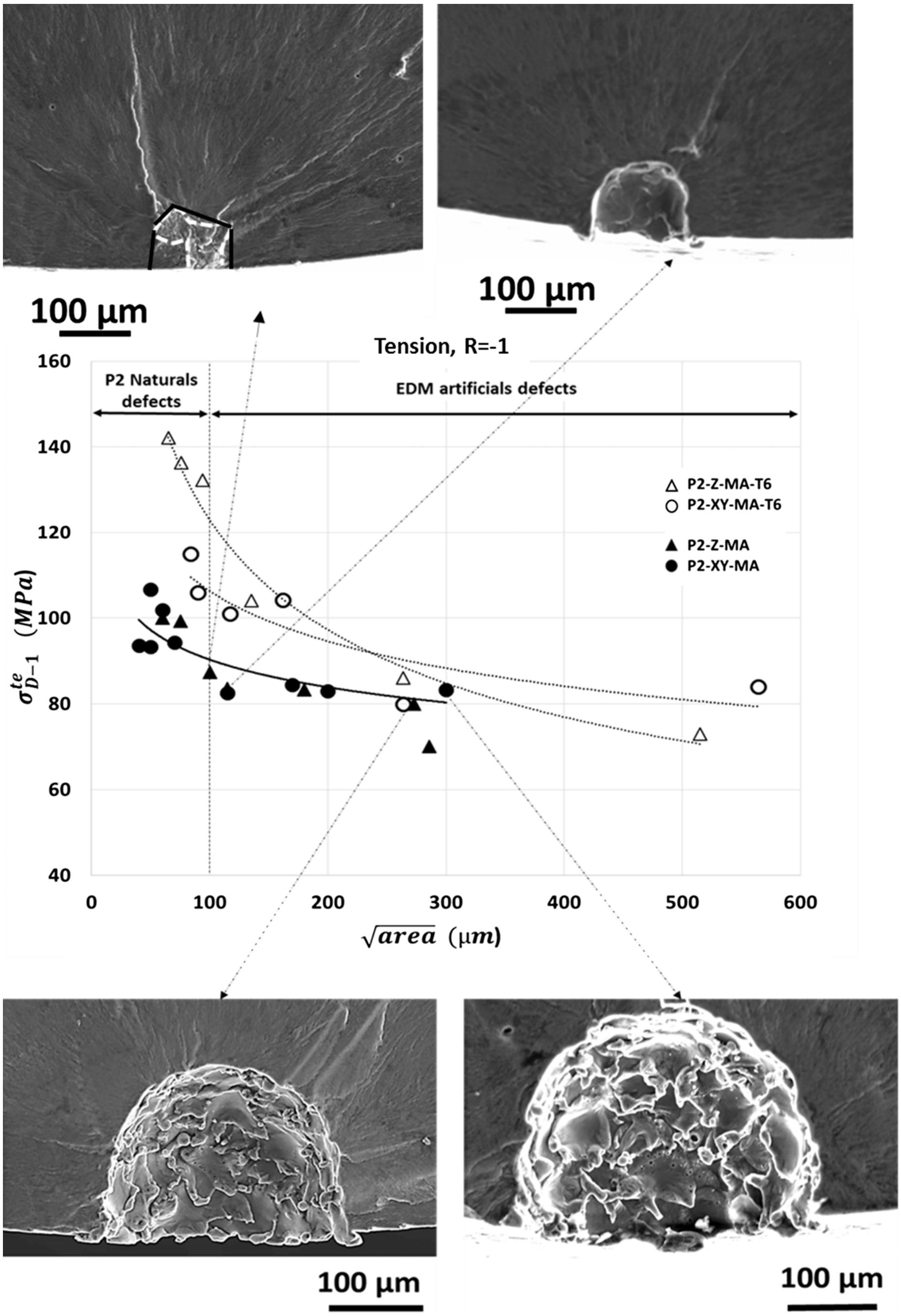

Fig. 12. Kitagawa type diagram showing the impact of defect size on the fatigue limit after or not heat treatment for two building direction XY and Z.

TEM analysis illustrated in Fig. 13 shows that dislocations are locked by the Si precipitates and even intermetallic particles that appear after the T6 heat treatment. It is therefore suggested that these precipitates and intermetallic needles are not sheared by the fatigue crack.

Even though the T6 heat treatment increases the fatigue strength, it further reveals an influence of the building direction which is not yet fully explained in the literature. As shown in this study, the T6 heat treatment makes all the sources of anisotropy in microstructure disappear except the grains. Fig. 14 presents a sketch to explain the differences in fatigue resistance observed between XY and Z after T6. In fact, during fatigue in Z T6 specimen, the initiation phase could be enhanced by the fine grain size, contrary to XY T6. This phenomenon is still valid without T6 but Z as the eutectic silicon particles make easier the fatigue crack propagation [30], the presence of a silicon that decorates the melt-pools boundaries should be taken into account when the T6 is not performed. As a consequence, all things equal otherwise, the impact of melt-pools on the fatigue life could be studied as the SDAS in cast AlSi alloys. The reduction in fatigue strength would therefore be controlled by the size of the melt pools. Thus, prior to T6 heat treatment, in Z specimens, the beneficial effect of the grain morphology could be counterbalanced by the presence of the large melt-pools.

Despite the significant role of the microstructure on the fatigue behavior, it has been shown that the defect size is the first order parameter that controls the fatigue limit. Given that engineering parts

Table 5
Tensile properties and micro hardness.

	YS (MPa)	Rp 0.02 (MPa)	UTS (MPa)	A%	µHV
P1-XY-MA-T6	/	/	320	1.05	/
	/	/	320	1.1	/
P2-XY-MA	210	172	325	11	136 ± 28
	208	175	330	11	
P2-Z-MA	195	145	350	8	136 ± 24
	195	145	350	8	
P2-XY-MA-T6	275	/	330	14.3	178 ± 53
	285	/	345	15.7	
P2-Z-MA-T6	280	200	300	14.7	180 ± 50
	255	225	330	15.2	
Cast A356-T6 [32–40]	210–300	/	220–330	0.3–4.3	/

elaborated by ALM process will have to admit a certain size of defect, it is then necessary to get further insights into the relationship between the fatigue limit and the defect size. With this aim, the Kitagawa diagram is plotted in log-log scales. Furthermore, in order to compare to classical damage tolerance approach, the LEFM prediction is calculated by assuming that defect is equivalent to a pre-existing crack. The fatigue limit is related to the stress intensity factor threshold ΔK_{th} by the following equation:

$$\Delta\sigma = \frac{1}{Y}\frac{\Delta K_{th}}{\sqrt{\pi a}} \tag{4}$$

where Y is the shape factor of the crack, $\boldsymbol{a}$ is the defect size defined by the $\sqrt{area}$ parameter. The assumption of a semicircular crack front shape is considered here, so that Y is supposed to be constant and equal to 0.64. The fatigue limit is then calculated by considering a threshold value $\Delta K_{th} = 2\,\text{MPa} \times \text{m}^{1/2}$ obtained from da-dN/ΔK experimental curves test on a P2-Z-MA sample. Fig. 15 exhibits the fatigue limit as a function of the defect size and compared to conventional cast alloy [18,24,25,27,28,42]. Fig. 15 suggests that the deviation from LEFM predictions is larger at smaller defect sizes, meaning that small natural defects such as those encountered in this study cannot be considered as a crack propagating in mode I with a long crack threshold of ΔK_{th} of $2\,\text{MPa} \times \text{m}^{1/2}$. A short crack correction should be applied.

Compared to conventional cast alloys, Fig. 15 shows that for defect sizes below 100 µm, the ALM material is more resistant to fatigue.

5. Conclusions

This work describes the role of microstructure and defect on the fatigue life of an AlSi10MgSi alloy prepared by Additive Layer Manufacturing. The alloy was characterized and described using the following microstructural parameters: the melt-pools, the dendritic structure, the grains then, the precipitation and intermetallic particles, and the process inherited defects.

Due to T6 heat treatment, the diffusion of silicon in the matrix leads to the disappearance of the dendritic structure and melt-pools boundaries. At the same time pure silicon precipitates and Fe-contained, needle-shaped intermetallic particles are formed.

For non-heat treated machined samples, the tensile properties such as the ultimate tensile strength and ductility are strongly affected by the building direction while the T6 heat treatment tends to annihilate this effect and considerably increase the yield strength and ductility. Concerning the fatigue, two building directions was studied, with and without T6 heat treatment. In that way, the following conclusions can be drawn:

(1) Regardless if material where or not subjected to the T6 heat treatment, the defect size is the first order parameter that controls the fatigue limit.
(2) For non-heat-treated material, there is no impact of the building direction on fatigue resistance.
(3) After a T6 heat treatment, a significant effect of building direction on fatigue life is noticed to the benefit of Z specimen.
(4) Whatever the building direction, the T6 heat-treatment improves the fatigue resistance, especially at small defect sizes.

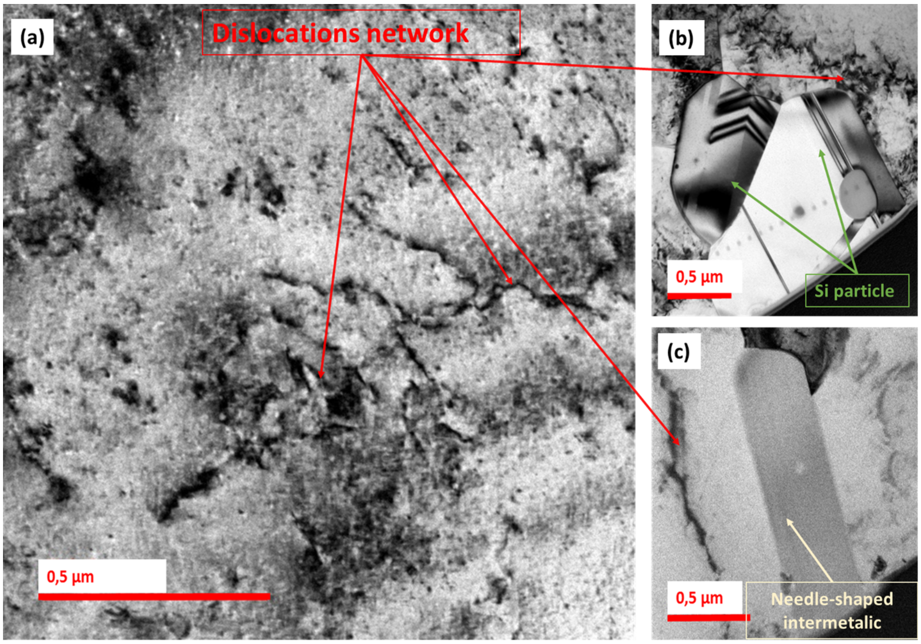

Fig. 13. TEM bright-field image of a thin foil removed from bulk T6 and fatigue tested specimen. (a) A matrix with a high dislocation density, (b) a twinned crystal of silicon containing no dislocations, (c) an intermetallic that is also dislocation-lean.

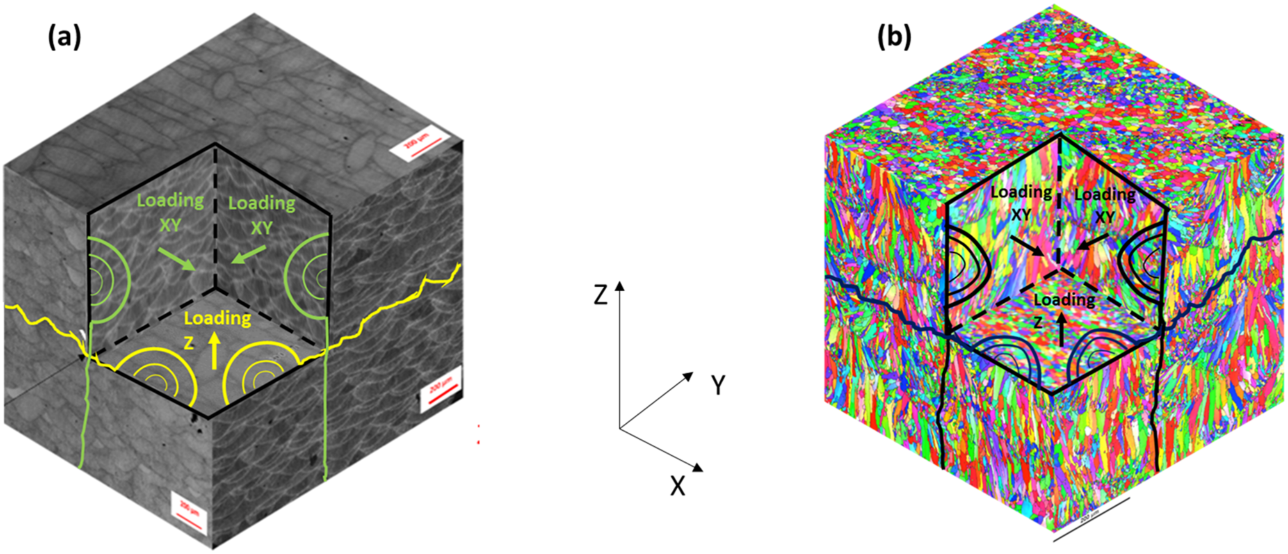

Fig. 14. Sketch explaining the difference observed on fatigue properties between XY and Z, (a) fatigue crack related to the melt-pools size, (b) fatigue crack related to the grain size.

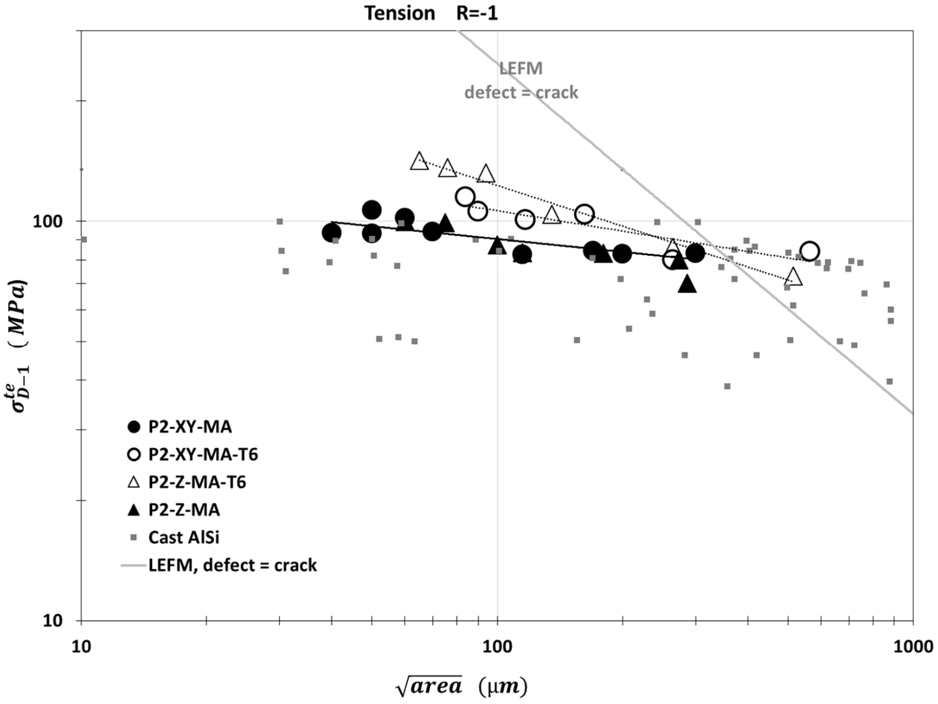

Fig. 15. Fatigue limit as a function of defect size, comparison between additive manufacturing and conventional cast alloys [18,24,25,27,28,42].

Acknowledgement

The authors gratefully acknowledges funding provided by Zodiac Aerospace and French National Research and Technology Association (ANRT). This work partially pertains to the French Government program “Investissements d'Avenir” (LABEX INTERACTIFS, reference ANR-11-LABX-0017-01). This work has been partially supported by « Nouvelle Aquitaine » Region and by European Structural and Investment Funds (ERDF reference: P-2016-BAFE-94/95). The authors acknowledge the facilities, and the scientific and technical assistance, of the Australian Centre for Microscopy and Microanalysis Research Facility at The University of Sydney. Finally the authors would like to thanks M. Monchatre and M. Brochu (Polytechnique Montreal) for performing the da-dN/ΔK experimental curves and Thierry Rouge-Carassat (Zodiac Engineering) for his comment on a present manuscript.

References

[1] Harun WSW, Kamariah MSIN, Muhamad N, Ghani SAC, Ahmad F, Mohamed Z. A review of powder additive manufacturing processes for metallic biomaterials. Powder Technol 2018;327:128–51. https://doi.org/10.1016/j.powtec.2017.12.058.

[2] Watson JK, Taminger KMB. A decision-support model for selecting additive manufacturing versus subtractive manufacturing based on energy consumption. J Clean Prod 2018;176:1316–22. https://doi.org/10.1016/j.jclepro.2015.12.009.

[3] Bose S, Ke D, Sahasrabudhe H, Bandyopadhyay A. Additive manufacturing of biomaterials. Prog Mater Sci 2018;93:45–111. https://doi.org/10.1016/j.pmatsci.2017.08.003.

[4] Bose S, Robertson SF, Bandyopadhyay A. Surface modification of biomaterials and biomedical devices using additive manufacturing. Acta Biomater 2018;66:6–22.

https://doi.org/10.1016/j.actbio.2017.11.003.

[5] Eyers DR, Potter AT. Industrial additive manufacturing: a manufacturing systems perspective. Comput Ind 2017;92–93:208–18. https://doi.org/10.1016/j.compind.2017.08.002.

[6] Olakanmi EO, Cochrane RF, Dalgarno KW. A review on selective laser sintering/melting (SLS/SLM) of aluminium alloy powders: processing, microstructure, and properties. Prog Mater Sci 2015;74:401–77. https://doi.org/10.1016/j.pmatsci.2015.03.002.

[7] Romano S, Brandão A, Gumpinger J, Gschweitl M, Beretta S. Qualification of AM parts: extreme value statistics applied to tomographic measurements. Mater Des 2017;131:32–48. https://doi.org/10.1016/j.matdes.2017.05.091.

[8] Portolés L, Jordá O, Jordá L, Uriondo A, Esperon-Miguez M, Perinpanayagam S. A qualification procedure to manufacture and repair aerospace parts with electron beam melting. J Manuf Syst 2016;41:65–75. https://doi.org/10.1016/j.jmsy.2016.07.002.

[9] Mardaras J, Emile P, Santgerma A. Airbus approach for F&DT stress justification of additive manufacturing parts. Proc Struct Integr 2017;7:109–15. https://doi.org/10.1016/j.prostr.2017.11.067.

[10] Thijs L, Kempen K, Kruth J-P, Van Humbeeck J. Fine-structured aluminium products with controllable texture by selective laser melting of pre-alloyed AlSi10Mg powder. Acta Mater 2013;61(5):1809–19. https://doi.org/10.1016/j.actamat.2012.11.052.

[11] Kempen K, Thijs L, Yasa E, Badrossamay M, Verheecke W, Kruth J-P. Process optimization and microstructural analysis for Selective Laser Melting of AlSi10Mg; 2011.

[12] Ming T. Inclusion, porosity, and fatigue of AlSi10Mg parts produced by selective laser melting. Melon University; 2017. Dissertation.

[13] Domfang Ngnekou JN, Nadot Y, Henaff G, Nicolai J, Ridosz L. Influence of defect size on the fatigue resistance of AlSi10Mg alloy elaborated by selective laser melting SLM. Proc Struct Integr 2017;7:75–83. https://doi.org/10.1016/j.prostr.2017.11.063.

[14] Takata N, Kodaira H, Sekizawa K, Suzuki A, Kobashi M. Change in microstructure of selectively laser melted AlSi10Mg alloy with heat treatments. Mater Sci Eng A 2017;704:218–28. https://doi.org/10.1016/j.msea.2017.08.029.

[15] Brandl E, Heckenberger U, Holzinger V, Buchbinder D. Additive manufactured AlSi10Mg samples using Selective Laser Melting (SLM): microstructure, high cycle fatigue, and fracture behavior. Mater Des 2012;34:159–69. https://doi.org/10.1016/j.matdes.2011.07.067.

[16] Maskery I, Aboulkhair NT, Truck C, Wildman RD. Fatigue performance enhancement of selective laser melted aluminium alloy by heat treatment; 2016.

[17] Aboulkhair NT, Maskery I, Tuck C, Ashcroft I, Everitt NM. Improving the fatigue behaviour of a selectively laser melted aluminium alloy: influence of heat treatment and surface quality. Mater Des 2016;104:174–82. https://doi.org/10.1016/j.matdes.2016.05.041.

[18] Beretta S, Romano S. A comparison of fatigue strength sensitivity to defects for materials manufactured by AM or traditional processes. Int J Fatigue 2017;94:178–91. https://doi.org/10.1016/j.ijfatigue.2016.06.020.

[19] Romano S, Brückner-Foit A, Brandão A, Gumpinger J, Ghidini T, Beretta S. Fatigue properties of AlSi10Mg obtained by additive manufacturing: defect-based modelling and prediction of fatigue strength. Eng Fract Mech 2018;187:165–89. https://doi.org/10.1016/j.engfracmech.2017.11.002.

[20] Siddique S, Imran M, Walther F. Very high cycle fatigue and fatigue crack propagation behavior of selective laser melted AlSi12 alloy. Int J Fatigue 2017;94:246–54. https://doi.org/10.1016/j.ijfatigue.2016.06.003.

[21] Buchbinder D, Meiners W. Generative Fertigung von Aluminiumbauteilen für die Serienproduktion. Förderkennzeichen 01RI0639A-D. Aachen Fraunhofer Inst. Laser Technol. ILT; 2010. p. 1–148. https://doi.org/10.2314/GBV:667761012.

[22] Yang KV, Rometsch P, Jarvis T, Rao J, Cao S, Davies C, Wu X. Porosity formation mechanisms and fatigue response in Al-Si-Mg alloys made by selective laser melting. Mater Sci Eng A 2018;712(September):166–74. https://doi.org/10.1016/j.msea.2017.11.078.

[23] Damon J, Dietrich S, Vollert F, Gibmeier J, Schulze V. Process dependent porosity and the influence of shot peening on porosity morphology regarding selective laser melted AlSi10Mg parts. Addit Manuf 2018;20(January):77–89. https://doi.org/10.1016/j.addma.2018.01.001.

[24] Houria MI. Experimental investigation and modeling the fatigue life of a cast aluminium alloy A356-T6 under multiaxial loading. France: Université de Poitiers; 2015. Thesis (in french).

[25] Roy M, Nadot Y, Maijer DM, Benoit G. Multiaxial fatigue behaviour of A356–T6. Fatigue Fract Eng Mater Struct 2012;35(12):1148–59. https://doi.org/10.1111/j.1460-2695.2012.01702.x.

[26] Li W, Li S, Liu J, Zhang A, Zhou Y, Wei Q, et al. Effect of heat treatment on AlSi10Mg alloy fabricated by selective laser melting: microstructure evolution, mechanical properties and fracture mechanism. Mater Sci Eng A 2016;663:116–25. https://doi.org/10.1016/j.msea.2016.03.088.

[27] Iben Houria M, Nadot Y, Fathallah R, Roy M, Maijer DM. Influence of casting defect and SDAS on the multiaxial fatigue behaviour of A356–T6 alloy including mean stress effect. Int J Fatigue 2015;80:90–102. https://doi.org/10.1016/j.ijfatigue.2015.05.012.

[28] Rotella A, Nadot Y, Piellard M, Augustin R. Influence of natural defects on the fatigue limit of a cast Al-Si alloy. Proc Struct Integr 2017;7:513–20. https://doi.org/10.1016/j.prostr.2017.11.120.

[29] Linder J, Axelsson M, Nilsson H. The influence of porosity on the fatigue life for sand and permanent mould cast aluminium. Int J Fatigue 2006;28(12):1752–8. https://doi.org/10.1016/j.ijfatigue.2006.01.001.

[30] Yi JZ, Gao YX, Lee PD, Lindley TC. Effect of Fe-content on fatigue crack initiation and propagation in a cast aluminum–silicon alloy (A356–T6). Mater Sci Eng A 2004;386(1–2):396–407. https://doi.org/10.1016/j.msea.2004.07.044.

[31] Wang Q, Apelian D, Lados D. Fatigue behavior of A356–T6 aluminum cast alloys. Part I. Effect of casting defects. J Light Met 2001;1(1):73–84. https://doi.org/10.1016/S1471-5317(00)00008-0.

[32] Sonsino C, Ziese J. Fatigue strength and applications of cast aluminium alloys with different degrees of porosity. Int J Fatigue 1993;15(2):75–84. https://doi.org/10.1016/0142-1123(93)90001-7.

[33] Jiang W, Fan Z, Liu D. Microstructure, tensile properties and fractography of A356 alloy under as-cast and T6 obtained with expendable pattern shell casting process. Trans Nonferrous Met Soc China 2012;22:s7–13. https://doi.org/10.1016/S1003-6326(12)61676-8.

[34] Lee MH, Kim JJ, Kim KH, Kim NJ, Lee S, Lee EW. Effects of HIPping on high-cycle fatigue properties of investment cast A356 aluminum alloys. Mater Sci Eng A 2003;340(1–2):123–9. https://doi.org/10.1016/S0921-5093(02)00157-0.

[35] Ran G, Zhou J, Wang QG. The effect of hot isostatic pressing on the microstructure and tensile properties of an unmodified A356–T6 cast aluminum alloy. J Alloys Compd 2006;421(1–2):80–6. https://doi.org/10.1016/j.jallcom.2005.11.019.

[36] Kim D-K, Hwang J-H, Kim E-Y, Heo Y-U, Woo W, Choi S-H. Evaluation of the stress-strain relationship of constituent phases in AlSi10Mg alloy produced by selective laser melting using crystal plasticity FEM. J Alloys Compd 2017;714:687–97. https://doi.org/10.1016/j.jallcom.2017.04.264.

[37] Ceschini L, Morri A, Sambogna G. The effect of hot isostatic pressing on the fatigue behaviour of sand-cast A356–T6 and A204–T6 aluminum alloys. J Mater Process Technol 2008;204(1–3):231–8. https://doi.org/10.1016/j.jmatprotec.2007.11.067.

[38] Gao YX, Yi JZ, Lee PD, Lindley TC. The effect of porosity on the fatigue life of cast aluminium-silicon alloys*. Fract Eng Mater Struct 2004;27(7):559–70. https://doi.org/10.1111/j.1460-2695.2004.00780.x.

[39] Murakami Y, Endo M. Effects of defects, inclusions and inhomogeneities on fatigue strength. Int J Fatigue 1994;16(3):163–82. https://doi.org/10.1016/0142-1123(94)90001-9.

[40] Kempen K, Thijs L, Van Humbeeck J, Kruth J-P. Mechanical properties of AlSi10Mg produced by selective laser melting. Phys Proc 2012;39:439–46. https://doi.org/10.1016/j.phpro.2012.10.059.

[41] Rice JR, Tracey DM. On the ductile enlargement of voids in triaxial stress fields∗. J Mech Phys Solids 1969;17(3):201–17. https://doi.org/10.1016/0022-5096(69)90033-7.

[42] Roy MJ, Nadot Y, Nadot-Martin C, Bardin PG, Maijer DM. Multiaxial Kitagawa analysis of A356–T6. Int J Fatigue 2011;33(6):823–32. https://doi.org/10.1016/j.ijfatigue.2010.12.011.

[42] Lin YC, Luo S-C, Huang J, Yin L-X, Jiang X-Y. Effects of solution treatment on microstructures and micro-hardness of a Sr-modified Al-Si-Mg alloy. Mater Sci Eng A 2018;725(February):530–40. https://doi.org/10.1016/j.msea.2018.04.049.